

# Three-component Stäckel model of the Galaxy based on the rotation curve from maser data

A. O.Gromov\*, I.I. Nikiforov

St. Petersburg State University, St. Petersburg, 198504 Russia

## Abstract

A three-component Stäckel model of the Galaxy, including the bulge, disk, and halo, is constructed. Parameter estimates of the potential are obtained as a result of fitting the model rotation curve to azimuthal velocities found from data on trigonometric parallaxes and spatial velocities of masers. The fitting method takes into account the measurement and natural dispersions of azimuthal velocities and uses an algorithm for excluding objects with excessive residuals. In order to obtain more uniform samples, the objects were divided into two groups: masers associated with high-mass star forming regions and masers of other types. A significant kinematic inhomogeneity of these groups was identified and taken into account: the azimuthal velocity dispersion is  $\sigma_{0,1} = 4.3 \pm 0.4 \text{ km s}^{-1}$ , in the first group and  $\sigma_{0,2} = 15.2 \pm 1.3 \text{ km s}^{-1}$  in the second. After constructing the model of the Galactic-plane potential, it was generalized to the entire space under the assumption of the existence of a third quadratic integral of motion. When reconstructing the Galactic rotation curve in detail, the used algorithm gives an analytical expression for the Stäckel potential, which significantly simplifies the task of constructing the Galaxy's phase density model in the Stäckel approximation. In order to make the Stäckel model more realistic, one needs to develop methods of direct account of data on the vertical distribution of density in the Galaxy.

Keywords: methods: analytical — methods: data analysis — Galaxy: structure — Galaxy: kinematics and dynamics

## 1. INTRODUCTION

Stäckel models are widely discussed in papers related in one way or another to constructing phase models of star systems, including those of our Galaxy. This is due to the possibility of the existence in such models of a third integral of motion, quadratic in velocity (in addition to the two classical integrals of energy and areas)

$$I_3 = (Rv_z - zv_R)^2 + z^2v_\lambda^2 + z_0^2(v_z^2 - 2\Phi^*) , \quad (1)$$

---

\*e-mail: granat08@yandex.ru

where

$$z_0^2 \frac{\partial \Phi^*}{\partial R} = z^2 \frac{\partial \Phi}{\partial R} - Rz \frac{\partial \Phi}{\partial z},$$

$$z_0^2 \frac{\partial \Phi^*}{\partial z} = (R^2 + z_0^2) \frac{\partial \Phi}{\partial z} - Rz \frac{\partial \Phi}{\partial R}.$$

Here  $R$ ,  $\lambda$ ,  $z$  are the cylindrical coordinates,  $\Phi$  is the potential of the model considered, and  $z_0$  is some constant of the dimension of length.

Such an integral is widely applied in stellar dynamics, for example, in the works of Kuzmin (1952), Kuzmin and Malasidze (1987), Osipkov (1975) and many other authors.

The velocity ellipsoid for most subsystems in the Galaxy, determined from the proper motions and radial velocities of the stars, is triaxial (see, e.g., the data on the principal velocity dispersions of main sequence stars with various  $B-V$  color indices in a monograph by Binney and Merrifield (1998)). One of the ellipsoid axes coincides with the  $v_\lambda$  axis. If the phase density depends on three integrals of motion, then this fact can be explained within the framework of the stationary Galaxy theory. Additionally, for models with three integrals of motion, the problem of computing orbits can be solved in quadratures. Since the radial velocity dispersion exceeds significantly the vertical one not only for nearby stars but also for objects representing a large interval of galactocentric distances (e.g., Bond et al., 2010; Rastorguev et al., 2017), hereinafter we shall assume for the entire Galaxy the existence of a global third integral as a phase density argument. Note that the choice of parameter  $z_0$  (see Section 4), the possible variations of which represent the difference in the local integrals for individual stars, can be considered as a selection of some average  $z_0$  for the latter, which even in this case allows us to talk about some common quasi integral of motion.

For practical purposes, one should consider only the single-valued integrals of motion: if non-isolating integrals become arguments of phase density, then it becomes infinitely multivalued, which lacks physical sense (see, e.g., the monograph by Ogorodnikov, 1958). Hénon and Heiles (1964) have shown numerically that when energy reaches some critical value, ergodic areas are formed where the third integral becomes non-isolating. Rodionov (1974) determined that in order to avoid such «ergodic layers» a sixfold continuous differentiability of the potential at the center of the system is needed.

The possibility of the existence of such third integrals has also been considered for other galaxies (e.g., Binney et al., 1990; Merrifield, 1991).

The condition of the existence of the third quadratic integral of motion (1) is written in the form of

$$3 \left( z \frac{\partial \Phi}{\partial R} - R \frac{\partial \Phi}{\partial z} \right) - (R^2 + z_0^2 - z^2) \frac{\partial^2 \Phi}{\partial R \partial z} + Rz \left( \frac{\partial^2 \Phi}{\partial R^2} - \frac{\partial^2 \Phi}{\partial z^2} \right) = 0. \quad (2)$$

For further computations it is convenient to switch to elliptical coordinates:  $\xi_1 \in [1; \infty)$ ,  $\xi_2 \in [-1; 1]$ ,

$$R = z_0 \sqrt{(\xi_1^2 - 1)(1 - \xi_2^2)}, \quad z = z_0 \xi_1 \xi_2. \quad (3)$$

The limitation (2) can then be written as

$$\frac{\partial^2}{\partial \xi_1 \partial \xi_2} [(\xi_1^2 - \xi_2^2) \Phi] = 0, \quad (4)$$

and the potential, in turn, as follows:

$$\Phi = \frac{\varphi(\xi_1) - \varphi(\xi_2)}{\xi_1^2 - \xi_2^2}, \quad (5)$$

where  $\varphi(\xi)$  is an arbitrary function.

Expression (4) is the condition of separating the variables, which means that such potentials are separable, i.e., they allow one to separate the variables in the Hamilton–Jacobi equation. Stäckel (1890) was the first to introduce in his works a class of potentials that satisfy (5). They later became known as Stäckel potentials and were introduced into stellar dynamics by Eddington (1915).

Another advantage of Stäckel potentials in phase modeling is the ability to describe models in angle–action variables. Multiple expressions for phase density with such variables are encountered in the literature (e.g., Dehnen, 1999; Posti et al., 2015). The algorithm for determining the actions and angles in separable potentials (Stäckel potentials are one type of such potentials) was developed by J. Binney and his team. This approach replaced the method of constructing tori (Kaasalainen and Binney, 1994), which turned out to be inconvenient since it gives a dependence of the phase variables on actions and angles and not vice versa, as is required, and the method of adiabatic invariants by Binney (2010), which was satisfactory only for stars close to the equatorial plane.

To introduce the Stäckel potential into models, Sanders (2012), Binney (2012), Sanders and Binney (2016) use the «Stäckel fudge» algorithm, where the  $\varphi(\xi)$  function is an interpolation based on some number of orbital points in the assumption that the non-Stäckel potential in those points has the properties of the Stäckel one. However, this approach is approximate. Additionally, the  $z_0$  parameter changes from orbit to orbit in such an approach. Due to this, one can only talk of some local third integral, since the constancy requirement for  $z_0$  is key to keeping integral  $I_3$ . Which integral is the phase density argument in the case of a non-constant  $z_0$  is not quite clear.

Undoubtedly, studies within the framework of the Stäckel fudge have provided a large contribution to the development of star system phase modeling methods. However, since global integrals should, strictly speaking, be phase density arguments, we suggest that an alternative approach based on the  $I_3$  integral with constant  $z_0$ , as another variant of fitting a more complex reality, is also of interest. In contrast to the numerical multi-step Stäckel fudge algorithm, such an approach is analytical and more simple. This paper is dedicated to the attempt to implement this analytical approach. The future will show which method will prove to be more accurate and convenient.

The first step to construct a phase model is obtaining the model of the potential that

is consistent with observations. Unfortunately, there are only a few studies where Stäckel potentials are constructed based on observations. One of the first was the work of Satoh and Miyamoto (1976), where a one-component model of the Galaxy was determined by the data on Galactic rotation and by the density in the solar vicinity. However, that study uses only 18 objects with distances up to 10 kpc. Additionally, the paper by Satoh and Miyamoto (1976) adopts the value  $\rho_{\odot} = 0.148 M_{\odot} pc^{-3}$ , which does not correspond to the contemporary results (Bland-Hawthorn and Gerhard, 2016; Loktin and Marsakov, 2009).

In a later work, Famaey and Dejonghe (2003) constructed Stäckel models of the Galaxy based on the derivatives, mainly local, of the dynamical characteristics (local circular velocity, flat rotation curve, Oort constants and others). Such models are only representative; in future, as Famaey and Dejonghe (2003) themselves note, more extensive kinematic data should be used, but such work has not been undertaken.

Formally, the models presented in Famaey and Dejonghe (2003) are three-component, however, the third component only appears in them due to an addition, mainly for demonstrative purposes, of a thick disk component to the spheroid and (thin) disk, the dynamic contribution of which is small compared to the thin disk (Bland-Hawthorn and Gerhard, 2016).

We should also note the paper by Binney and Wong (2017), where the «Stäckel fudge» algorithm is applied to data on Galactic globular clusters and a phase model is constructed for that cluster system. However, as was mentioned above, using the «Stäckel fudge» algorithm gives only an approximation of the Stäckel model.

This work, where we implement an analytical approach to constructing the Stäckel model for the Galaxy, is the first in a series of papers which as the end result aims to construct a phase model of the Galaxy which agrees with the large amount of information obtained from observations. Based on kinematic data on masers with trigonometric parallaxes we find the optimal parameters for the model potential in the Galactic plane, which we then generalize to three dimensions in the assumption of the existence of a third quadratic integral of motion. As a result we construct a three-component (halo, disk, bulge) Stäckel model of the Galaxy based on the current rotation data; we then discuss the feasibility of this model.

## 2. METHOD

Stäckel models of the Galaxy constructed in the papers mentioned above are merely approximate (representative or roughly Stäckel). The problem may be solved by a method proposed by Rodionov (1974), which allows one to generalize the equatorial plane potential to the entire space in the Stäckel way, obtaining an analytical expression as a result. Since no limitations are applied in this case to the equatorial plane potential, any model may be used to construct the Stäckel model, for example, one obtained by approximating the

data on the rotation of the «cool» Galactic subsystem encompassing a large interval of distances  $R$ . In particular, one can use maser data, and, as a possibility, the Gaia catalog.

If the potential in set in the equatorial plane,  $\varphi(\xi)$  is determined as (Rodionov, 1974):

$$\varphi(\xi) = \xi^2 \Phi \left( R = z_0 \sqrt{|\xi^2 - 1|}, z = 0 \right). \quad (6)$$

Such a choice of function  $\varphi(\xi)$  facilitates the fulfillment of the following conditions:

- 1)  $\varphi(0) = 0$ ;
- 2)  $\varphi(1) = \Phi_0$ , where  $\Phi_0$  — is the potential in the center of the model;
- 3) when  $\xi \rightarrow \infty$   $\frac{\varphi(\xi)}{\xi} \rightarrow \frac{GM}{z_0}$ , where  $G$  — is the gravitational constant and,  $M$  — is the total mass.

The author of the method (Rodionov, 1974) also proposed ways to estimate the function  $\varphi(\xi)$ , if the potential is defined on the  $z$  and in an arbitrary column  $(R_*, z)$ , where  $R_* = \text{const}$ .

We used this method earlier to construct one- and two-component Stäckel test models of the Galaxy (Gromov et al., 2015, 2016). We used the data on neutral hydrogen rotation as well as those on masers. A good agreement between model rotation curves and observed data was obtained, and also between model values and estimates of density in the solar vicinity, mass in a sphere of 50 kpc radius and other dynamic characteristics.

In this work we use the same method to construct a more realistic three-component Stäckel model of the Galaxy with the classical composition: halo, disk, and bulge. Since the goal is to determine the applicability of Rodionov's method in a separate representation of the main dynamic components of the Galaxy in the model, further refinement of the model (for instance, adding a thick disk) seems excessive at this stage.

We chose a quasi-isothermal potential proposed in Kuzmin et al. (1986) to describe the halo:

$$\Phi_1(R, 0) = \Phi_{0,1} \ln \left( 1 + \frac{\beta}{w(R)} \right), \quad (7)$$

where the  $w(R)$  function is determined as:

$$w^2(R) = 1 + \kappa_1^2 R^2.$$

The disk is presented as a general isochronous potential (Kuzmin and Malasidze, 1969):

$$\Phi_2(R, 0) = \Phi_{0,2} \frac{\alpha}{(\alpha - 1) + \sqrt{1 + \kappa_2^2 R^2}}. \quad (8)$$

To describe the central bulge we used the Hernquist potential (Hernquist, 1990):

$$\Phi_3(R, 0) = \Phi_{0,3} \frac{1}{R + \kappa_3}. \quad (9)$$

Table 1: List of additional maser sources from the catalog of Rastorguev et al. (2017), which belong to high-mass starforming regions (HMSFRs) according to Nikiforov and Veselova (2018)

|               |                |
|---------------|----------------|
| G170.66−00.25 | G059.83+00.67  |
| G213.70−12.60 | G071.52−00.38  |
| G054.10−00.08 | G305.200+0.019 |
| G058.77+00.64 | G305.202+0.208 |
| G059.47−00.18 |                |

According to (6) the function  $\varphi_i(\xi)$  for individual components has the following form:

$$\varphi_1(\xi) = \xi^2 \Phi_{0,1} \ln \left( 1 + \frac{\beta}{\sqrt{1 + \kappa_1^2 z_0^2 |\xi^2 - 1|}} \right), \quad (10)$$

$$\varphi_2(\xi) = \xi^2 \Phi_{0,2} \frac{\alpha}{(\alpha - 1) + \sqrt{1 + \kappa_2^2 z_0^2 |\xi^2 - 1|}}, \quad (11)$$

$$\varphi_3(\xi) = \xi^2 \Phi_{0,3} \frac{1}{\sqrt{z_0^2 |\xi^2 - 1|} + \kappa_3}. \quad (12)$$

As a result, the final expression for the Stäckel potential function

$$\varphi(\xi) = \varphi_1(\xi) + \varphi_2(\xi) + \varphi_3(\xi) \quad (13)$$

is analytical, which allows us to find the function value and, as a consequence, the values of the action variables in the entire region of defined phase coordinates, and not in isolated points. The values of  $\varphi(\xi)$  are determined exactly here, and the accuracy of determining the action variables that are expressed through complex integrals is limited only by the accuracy of the numerical methods used to find the latter.

### 3. OBSERVED DATA

In this work we use data on masers located in star forming regions. VLBI observations allow one to obtain accurate estimates of trigonometric parallaxes and proper motions, including even for maser sources that are rather distant from the Sun ( $r < 10$  kpc) (Nikiforov and Veselova, 2018).

We used the catalog from Rastorguev et al. (2017) as the main maser database, which includes 103 high-mass star forming regions (HMSFRs) from the homogeneous catalog of Reid et al. (2014) and 38 additional maser sources of which, as determined by Nikiforov and Veselova (2018), nine belong to the HMSFR class (see Table 1), and the remaining ones are of other types (hereafter non-HMSFR masers). Furthermore, we added another 3 masers with full data: Sh2-76EMM1, Sh2-76EMM2 (G040.44+02.45) and AFGL 5142 (G174.20-00.07); they all belong to the non-HMSFR group. The total sample thus consists of 144 objects

As was shown by Nikiforov and Veselova (2018), the measurement uncertainty for non-HMSFR maser parallaxes is on average higher than for the HMSFR masers. Additionally, unlike the HMSFR sources belonging to the same class of objects, non-HMSFR masers belong to 14 different classes (Nikiforov and Veselova, 2018). This fact allows us to assume that the sample uniting these objects is kinematically inhomogeneous. We therefore differentiated between HMSFR (112 objects) and non-HMSFR (32 objects) masers when processing data in the general case. In particular, dynamic modeling was carried out separately for the more homogeneous HMSFR group and for the joint (HMSFR + non-HMSFR) sample. We did not consider the non-HMSFR sample separately, since its volume is insufficient for completing the outlined task. As we show below, HMSFR and non-HMSFR masers are indeed kinematically inhomogeneous with respect to each other.

## 4. PARAMETER OPTIMIZATION

The parameters of the model potential described in Section 2 were estimated using the nonlinear least squares method. The residual for an individual object was the difference between the model circular velocity  $\theta_C(R_i)$ , where  $R_i$  is the galactocentric distance of the said object, and azimuthal velocity  $\theta_i$ , computed by the measured position and three velocity components of the object (see details in Gromov et al. (2016)<sup>1</sup>). Since the natural azimuthal velocity dispersion of masers was considered as a-priori unknown, at the initial stage we minimized the objective function

$$L^2 = \sum_{i=1}^N p_i [\theta_i - \theta_C(R_i)]^2, \quad (14)$$

where

$$p_i = \frac{1}{\sigma_i^2}, \quad (15)$$

is the weight of the  $i$ th object that accounts only for the measurement uncertainty  $\sigma_i$  of velocity  $\theta_i$  (see Gromov et al. (2016));  $\theta_C = -R \frac{d\Phi}{dR}$ ,  $\Phi(R, 0) = \Phi_1(R, 0) + \Phi_2(R, 0) + \Phi_3(R, 0)$ ;  $N$  is the volume of the sample considered.

The parameter estimates for HMSFR masers and for those of the joint sample, obtained by minimizing (14) are presented in Table 2, the corresponding model rotation curves are fitted to the observed data in Fig 1. Since some computation versions in this work have limiting parameter  $\beta$  values —  $\beta \rightarrow \infty$  (in this case the quasi-isothermal potential becomes the Schuster–Plummer potential),— the associated parameter  $q = \frac{\beta}{\beta + 1} \in [0; 1)$  was estimated instead.

When minimizing (14) with weights (15) the values of  $L^2/N_{\text{free}}$  (reduced statistics  $\chi^2$ ), where  $N_{\text{free}} = N - M$  is the number of degrees of freedom,  $M$  is the number of parameters to be determined, turned out to be much larger than unity (Table 2). This implies that

---

<sup>1</sup>In item 7 of the Appendix in Gromov et al. (2016) the correct formula is  $\sin \beta = \frac{r \cos b}{R} \sin l$ .

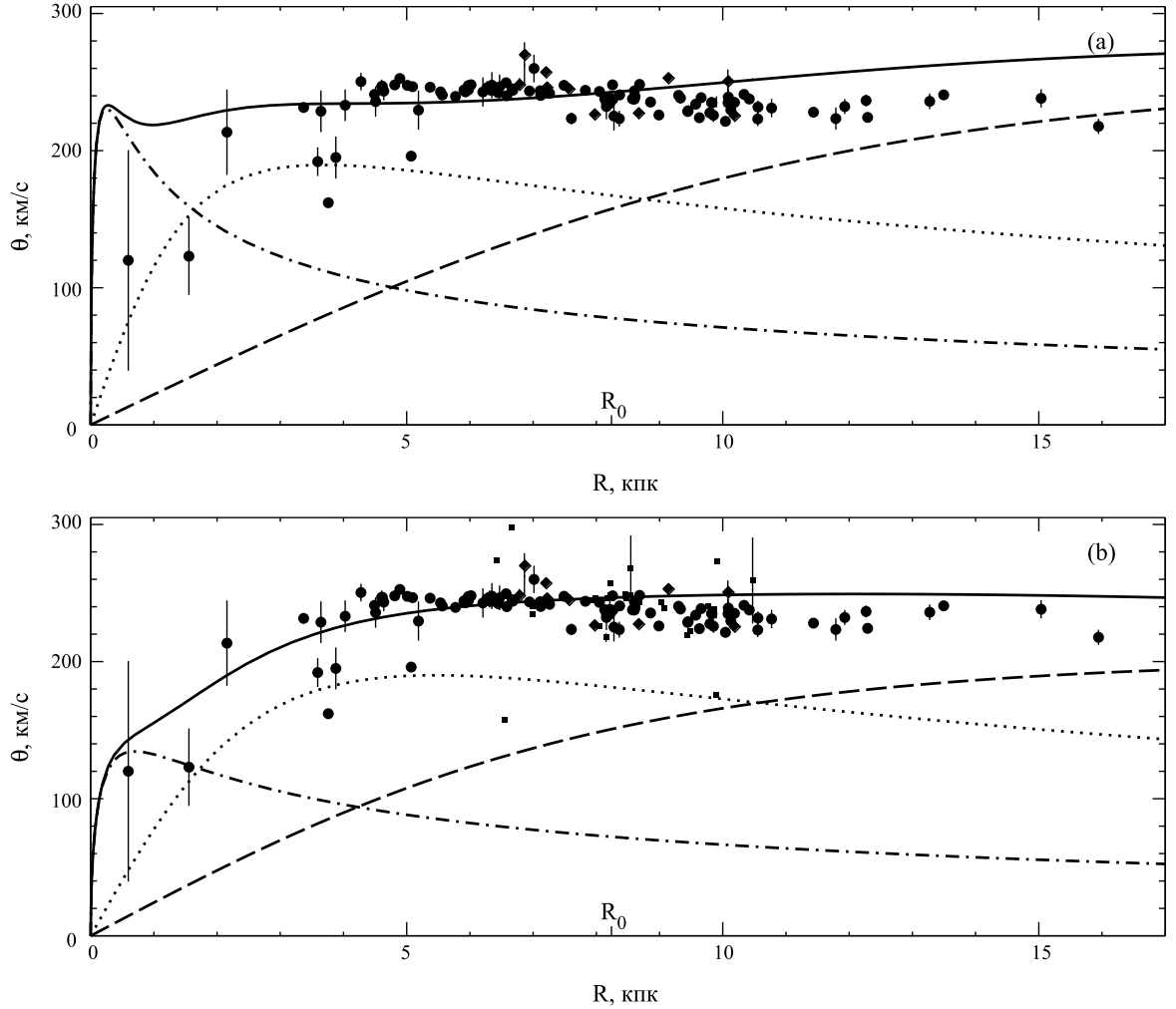


Figure 1: Model circular velocity curves, obtained without account of the natural dispersion of azimuthal velocities: from HMSFR masers (a), from a joint HMSFR + non-HMSFR sample (b). The solid curve is the three-component model of the Galaxy; the dashed curve shows the quasi-isothermal component representing the halo; the dotted line is the general isochronous component that describes the disk; the dashed-and-dotted curve is the Hernquist component representing the bulge. Also shown are the maser azimuthal velocities found from their measured parallaxes, radial velocities, and proper motions. The circles show the HMSFR masers from the catalog of Reid et al. (2014); rhombi show the HMSFR masers from the additional list in Rastorguev et al. (2017); small squares show the non-HMSFR masers from the list of Rastorguev et al. (2017) (they have little effect on the solution). The bars show the initial data measurement errors. The absence of a bar means that it is smaller than the size of the symbol representing the object. The horizontal axis shows the distance of the Sun from the center of the Galaxy adopted in this work,  $R_0 = 8.34$  kpc Reid et al. (2014).

Table 2: Solution without account for the natural azimuthal velocity dispersion

| Characteristic                          | HMSFRs              | HMSFRs +<br>non-HMSFRs |
|---|---------------------|------------------------|
| $N$                                     | 112                 | 144                    |
| $q$                                     | $0.6748 \pm 0.0073$ | $0.8421 \pm 0.0022$    |
| $\kappa_1, \text{kpc}^{-1}$             | $0.0611 \pm 0.0013$ | $0.2888 \pm 0.0035$    |
| $\Phi_{0,1}, \text{km}^2 \text{s}^{-2}$ | $305.5 \pm 6.5$     | $262.8 \pm 1.1$        |
| $\alpha$                                | $1.214 \pm 0.023$   | $1.240 \pm 0.019$      |
| $\kappa_2, \text{kpc}^{-1}$             | $0.533 \pm 0.015$   | $0.10102 \pm 0.00029$  |
| $\Phi_{0,2}, \text{km}^2 \text{s}^{-2}$ | $400.6 \pm 5.0$     | $310.83 \pm 0.97$      |
| $\Phi_{0,3}, \text{km}^2 \text{s}^{-2}$ | $230.4 \pm 14.3$    | $233.7 \pm 3.7$        |
| $\kappa_3, \text{kpc}$                  | $0.25 \pm 0.12$     | $0.70 \pm 0.24$        |
| $L^2/N_{\text{free}}$                   | 236                 | 713                    |

the deviations of azimuthal velocities  $\theta_i$  of masers from the model cannot be explained only by measurement errors, and therefore, the natural velocity dispersion has to be taken into account even for such the «cool» disk subsystem as masers (in accordance with the results of Rastorguev et al., 2017).

Therefore, at the second stage, the natural dispersion  $\sigma_0$  of maser azimuthal velocities was introduced into the objective function as an unknown parameter by writing the weight coefficients as:

$$p_i = (\sigma_i^2 + \sigma_0^2)^{-1}, \quad (16)$$

where  $\sigma_i$  — is the measurement uncertainty  $\theta_i$ .

The value  $\sigma_0$  was estimated in an iterative procedure, each step of which had fixed parameters of the potential determined in the previous step, and the natural dispersion was determined from the following equation:

$$L^2(\sigma_0^2) = N_{\text{free}}. \quad (17)$$

Using the  $\sigma_0$  obtained at this stage, the parameters of the potential were determined anew as a result of minimizing function (14) with the system of weights (16). The found parameter estimates were used in the next step to find a new approximation of  $\sigma_0$ . In all cases the procedure converged in three steps. As an initial approximation we took the result obtained with the system of weights (15).

To verify and account for the kinematic inhomogeneity of the non-HMSFR maser group with respect to the HMSFR group, in addition to the natural dispersion, common for the joint HMSFR + non-HMSFR sample (let us call this variant «approach 1»), we also estimated this dispersion for the HMSFR group,  $\sigma_{0,1}$ , and the non-HMSFR group,  $\sigma_{0,2}$ , individually (let us call this variant «approach 2»). In the latter case we used the weight coefficients  $p_{i,1} = (\sigma_i^2 + \sigma_{0,1}^2)^{-1}$  for the HMSFR objects, and  $p_{i,2} = (\sigma_i^2 + \sigma_{0,2}^2)^{-1}$  for non-HMSFR objects.

Table 3: Solution with account for the natural azimuthal velocity dispersions

| Characteristic                                    | HMSFRs              | HMSFRs + non-HMSFRs<br>(approach 1) | HMSFRs + non-HMSFRs<br>(approach 2) |
|---|---------------------|-------------------------------------|-------------------------------------|
| $N$   | 112                 | 144                                 | 144                                 |
| $\sigma_0$ or $\sigma_{0,1}$ , km s <sup>-1</sup> | 7.67 ± 0.74         | 12.1 ± 1.0                          | 7.59 ± 0.65                         |
| $\sigma_{0,2}$ , km s <sup>-1</sup>               |                     |                                     | 20.9 ± 1.8                          |
| $q$   | 1 <sub>-0.035</sub> | 1 <sub>-0.053</sub>                 | 1 <sub>-0.035</sub>                 |
| $\kappa_1$ , kpc <sup>-1</sup>                    | 0.0773 ± 0.0026     | 0.0734 ± 0.0031                     | 0.0956 ± 0.0032                     |
| $\Phi_{0,1}$ , km <sup>2</sup> s <sup>-2</sup>    | 265.2 ± 9.4         | 264.9 ± 15.1                        | 265.0 ± 10.2                        |
| $\alpha$  | 0.1437 ± 0.0041     | 0.1148 ± 0.0048                     | 0.1651 ± 0.0062                     |
| $\kappa_2$ , kpc <sup>-1</sup>                    | 0.0533 ± 0.0013     | 0.04686 ± 0.0016                    | 0.0504 ± 0.0012                     |
| $\Phi_{0,2}$ , km <sup>2</sup> s <sup>-2</sup>    | 311.2 ± 3.2         | 318.4 ± 4.1                         | 317.4 ± 3.2                         |
| $\Phi_{0,3}$ , km <sup>2</sup> s <sup>-2</sup>    | 224.5 ± 15.6        | 223.4 ± 20.1                        | 223.8 ± 15.7                        |
| $\kappa_3$ , kpc                                  | 0.71 ± 0.32         | 0.72 ± 0.34                         | 0.76 ± 0.31                         |

In the case of two natural dispersions equation (17) can be written as:

$$L^2 (\sigma_{0,1}^2, \sigma_{0,2}^2) = \sum_{i=1}^{N_1} \frac{[\theta_i - \theta_C(R_i)]^2}{\sigma_i^2 + \sigma_{0,1}^2} + \sum_{i=N_1+1}^N \frac{[\theta_i - \theta_C(R_i)]^2}{\sigma_i^2 + \sigma_{0,2}^2} = N_{\text{free}},$$

where the first sum is taken by the HMSFR objects, and the second — by the non-HMSFR objects. If the dispersions in the denominators of the two sums are correct, the contribution of each of them into the total result is asymptotically equal to the fraction of each group of objects in the joint sample. This gives the equations for determining  $\sigma_{0,1}$  and  $\sigma_{0,2}$ :

$$\sum_{i=1}^{N_1} p_{i,1} [\theta_i - \theta_C(R_i)]^2 = \frac{N_1}{N} N_{\text{free}}, \quad (18)$$

$$\sum_{i=N_1+1}^N p_{i,2} [\theta_i - \theta_C(R_i)]^2 = \frac{N_2}{N} N_{\text{free}}, \quad (19)$$

where  $N_1$  and  $N_2$  are the numbers of masers in HMSFR and non-HMSFR groups respectively,  $N = N_1 + N_2$ ; for the total sample  $N_1 = 112$ ,  $N_2 = 32$ ,  $N = 144$ . The  $\sigma_{0,1}$  and  $\sigma_{0,2}$  values were obtained as a result of an iterative procedure similar to the one described above.

The results obtained at the second stage are presented in Table 3 and Fig. 2.

The solution without account for the natural azimuthal velocity dispersion was unstable with respect to the sample composition (see the results for two samples in Table 2 and in Fig. 1), obviously, due to the exceedingly strong influence of objects with a high ratio of the absolute residual value to the (very small) measurement error (examples are evident in Fig. 1). Introducing the natural dispersion has, for the most part, eliminated this effect and stabilized the solution: all three results turned out to be close (Table 3, Fig. 2).

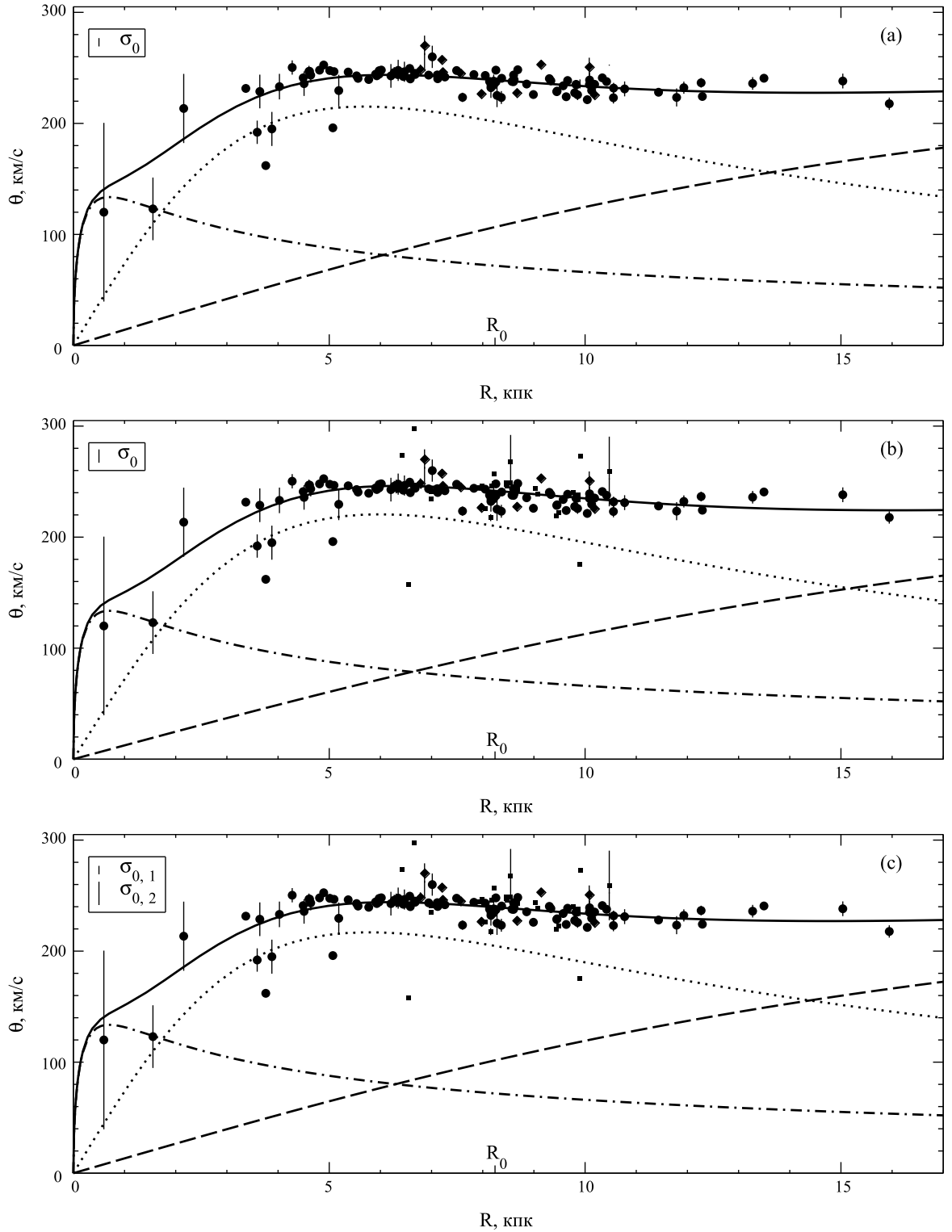


Figure 2: Same as in Fig. 1, but with account for the natural dispersion of azimuthal velocities: for the HMSFR sample (a), for the joint HMSFR + non-HMSFR sample with the same (b), and with different (c) natural dispersions for the HMSFR and non-HMSFR types. The top left parts of the panels show (in vertical axis scale) the bars of root-meansquare deviations corresponding to the derived natural dispersions.

Only the natural dispersions differ, and significantly: adding non-HMSFR masers to the sample increases  $\sigma_0$  by a factor of 1.5; direct dispersion measurements for the two maser groups show that  $\sigma_{0,2}$  is multiple times larger than  $\sigma_{0,1}$ . These facts imply a kinematic inhomogeneity of the joint sample and justify the introduction of two dispersions.

An analysis of the residuals of the derived solutions has shown that even after taking into account the natural dispersion, the sample still contains objects with data outliers, which can substantially shift the solution. To eliminate objects with excessive residuals at the third and final stage, we used the following algorithm with a flexible boundary for criterion statistics (Nikiforov, 2012). We searched for objects for which

$$\frac{|\theta_i - \theta_C(R_i)|}{\sqrt{\sigma_i^2 + \sigma_0^2}} > k, \quad (20)$$

where  $k$  is determined from the equation

$$[1 - \psi(k)] N_{\text{free}} = 1,$$

$\psi(z) = \sqrt{\frac{2}{\pi}} \int_0^z e^{-\frac{1}{2}t^2} dt$  is the probability integral and  $\sigma_0$  is the corresponding natural dispersion, i.e.  $\sigma_0$ ,  $\sigma_{0,1}$  or  $\sigma_{0,2}$  depending on the approach and object. Then out of  $L$  objects that satisfied the condition (20),  $L - L'$  object were excluded, where  $L' = 3$  at the stage of determining  $\sigma_0$ ,  $\sigma_{0,1}$ ,  $\sigma_{0,2}$  or  $L' = 1$  at the final stage of estimating model parameters with the derived (fixed) natural dispersions (see Nikiforov, 2012). Objects with absolute residual values exceeding  $k_{0.05}$ , i.e., the root of equation

$$[1 - \psi(k_{0.05})] N_{\text{free}} = 0.05,$$

were also excluded, if found among the remaining objects.

After each iteration of exclusions, the problems of parameter optimization, natural dispersion determination, and finding possible outliers in the data were solved anew until no object was excluded during the next iteration.

The object G110.19+02.47 with a negative residual  $< 3\sigma$ , which is not formally excessive according the criteria listed above, was also forcefully excluded within the framework of approach 2. However, it is isolated from the array of other non-HMSFR masers in the histogram of the distribution of relative residuals. This is the only object the class of which could not be determined from the original work of Chibueze et al. (2014). These authors also note the low azimuthal velocity of this object, linking it with the local kinematic anomaly, which does not characterize the Galaxy as a whole, of the Perseus arm in the region of the rotation curve  $R \sim 9$  kpc. Additionally, including this object in the sample noticeably increases  $\sigma_{0,2}$  from  $15.2 \pm 1.3$  (final estimate) to  $19.6 \pm 1.7$  km/s. Maser G110.19+02.47 was therefore excluded as a possibly anomalous object.

The list of excluded objects for the samples and approaches considered is shown in

Table 4: Lists of objects excluded from consideration in order of their exclusion during the final estimation of model parameters ( $L' = 1$ ). The critical values of  $k$  and  $k_{0.05}$  are shown for the final sample volumes

| Object                          | $\frac{ \theta_i - \theta_C(R_i) }{\sqrt{\sigma_i^2 + \sigma_{0,i}^2}}$ |
|---------------------------------|---|
| HMSFRs                          |   |
| ( $k = 2.59, k_{0.05} = 3.49$ ) |   |
| G348.70-01.04                   | 5.53  |
| G023.44-00.18                   | 4.01  |
| G213.70-12.60                   | 4.12  |
| HMSFRs+non-HMSFRs               |   |
| Approach 1                      |   |
| ( $k = 2.67, k_{0.05} = 3.55$ ) |   |
| G348.70-01.04                   | 3.75  |
| G110.10+02.47                   | 4.87  |
| G353.27+00.64                   | 4.28  |
| G173.72-02.70                   | 4.35  |
| G023.44-01.18                   | 4.14  |
| G045.37-00.22                   | 4.24  |
| G339.88-01.26                   | 3.80  |
| Approach 2                      |   |
| ( $k = 2.67, k_{0.05} = 3.56$ ) |   |
| G348.70-01.04                   | 5.83  |
| G110.10+02.47                   | —   |
| G353.27+00.64                   | 3.06  |
| G213.70-12.60                   | 4.00  |
| G023.44-01.18                   | 4.11  |
| G045.37-00.22                   | 4.13  |

Table 4. The final model parameter optimization results from the maser data are presented in Table 5 and in Fig. 3. Model component masses within a 50 kpc radius sphere are as follows:  $M_{\text{bulge}} = 1.1 \times 10^{10} M_{\odot}$ ,  $M_{\text{disk}} = 8.7 \times 10^{10} M_{\odot}$ ,  $M_{\text{halo}} = 7.2 \times 10^{11} M_{\odot}$ .

Parameter  $z_0$  of the Stäckel potential was determined from the following relation:

$$z_0^2(R) = \frac{3 \frac{\partial \Phi}{\partial R}(R, 0) + R \left[ \frac{\partial^2 \Phi}{\partial R^2}(R, 0) - 4 \frac{\partial^2 \Phi}{\partial z^2}(R, 0) \right]}{\frac{\partial^3 \Phi}{\partial z^2 \partial R}(R, 0)} - R^2. \quad (21)$$

Similar functions for  $z_0$  were constructed by Einasto and Rummel (1970), and also Osipkov (1975). We used the three-component potential from Gardner et al. (2011) as potential  $\Phi(R, z)$  to find  $z_0$  since data on the vertical structure of the Galaxy were used in its construction. The derived value  $z_0 = 5.3$  kpc agrees with the estimates presented in other papers:  $z_0 = 2.2 \div 7$  kpc (Hori, 1962; Kuzmin, 1953, 1956; Malasidze, 1973). We should note that some of these studies use distances to the center of the Galaxy  $R_0$ , that are lower

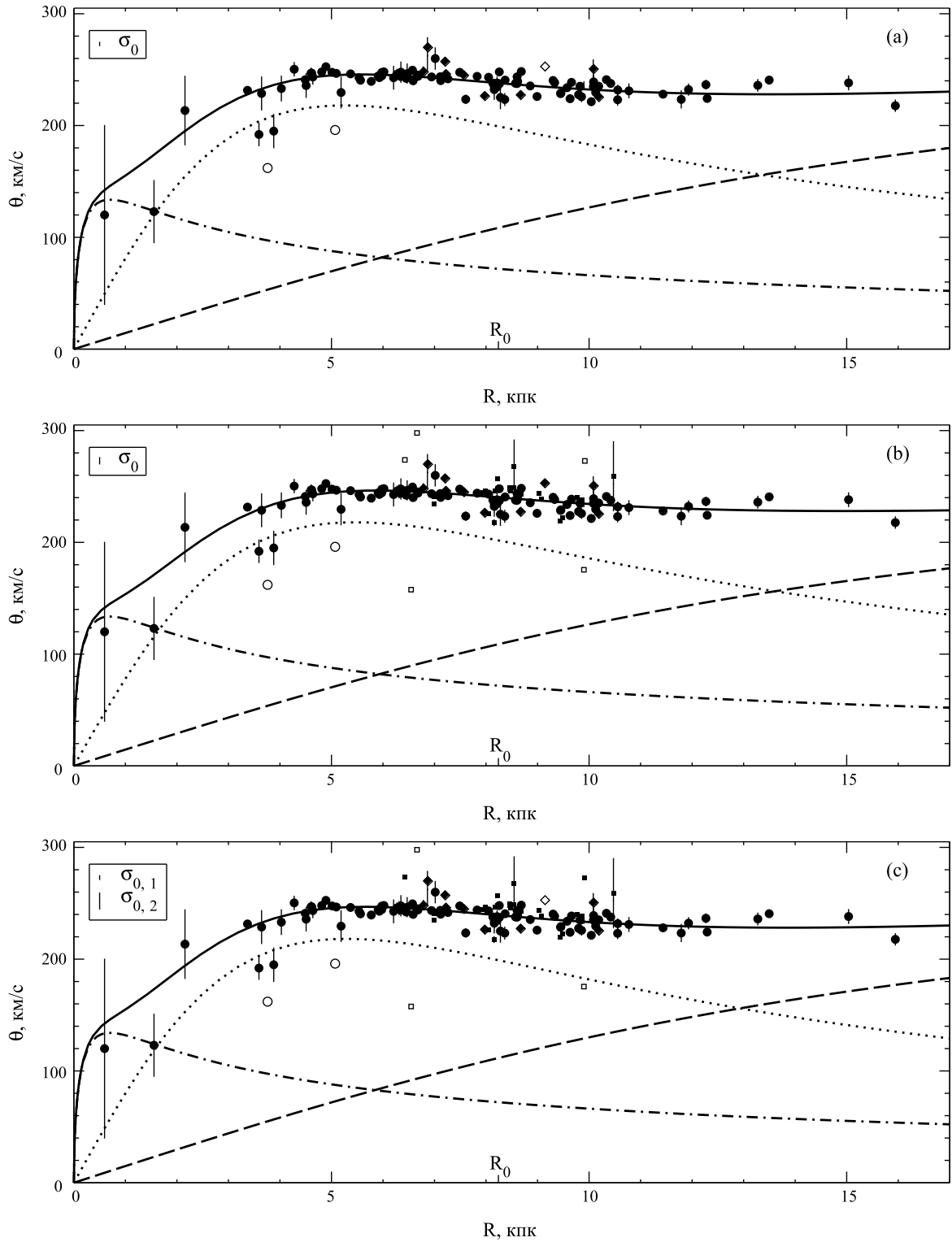


Figure 3: Same as in Fig. 2, but after excluding from consideration the masers with data outliers and the anomalous object. The open symbols show the discarded objects.

Table 5: Solution with account for the natural azimuthal velocity dispersion after excluding from consideration the masers with data outliers and the anomalous object

| Characteristic                                    | HMSFRs                | HMSFRs + non-HMSFRs<br>(approach 1) | HMSFRs + non-HMSFRs<br>(approach 2) |
|---|-----------------------|-------------------------------------|-------------------------------------|
| $N$   | 109                   | 137                                 | 138                                 |
| $\sigma_0$ or $\sigma_{0,1}$ , $\text{km s}^{-1}$ | $3.85 \pm 0.38$       | $6.56 \pm 0.57$                     | $4.34 \pm 0.38$                     |
| $\sigma_{0,2}$ , $\text{km s}^{-1}$               |                       |                                     | $15.2 \pm 1.3$                      |
| $q$   | $1_{-0.018}^{+0}$     | $0.943 \pm 0.023$                   | $1_{-0.014}^{+0}$                   |
| $\kappa_1$ , $\text{kpc}^{-1}$                    | $0.1173 \pm 0.0023$   | $0.1012 \pm 0.0025$                 | $0.0830 \pm 0.0020$                 |
| $\Phi_{0,1}$ , $\text{km}^2 \text{s}^{-2}$        | $264.6 \pm 6.0$       | $264.5 \pm 7.2$                     | $264.6 \pm 5.3$                     |
| $\alpha$  | $0.2495 \pm 0.0046$   | $0.1651 \pm 0.0046$                 | $0.1068 \pm 0.0031$                 |
| $\kappa_2$ , $\text{kpc}^{-1}$                    | $0.05455 \pm 0.00085$ | $0.0575 \pm 0.0011$                 | $0.05645 \pm 0.00055$               |
| $\Phi_{0,2}$ , $\text{km}^2 \text{s}^{-2}$        | $321.2 \pm 1.9$       | $318.9 \pm 3.1$                     | $315.6 \pm 1.7$                     |
| $\Phi_{0,3}$ , $\text{km}^2 \text{s}^{-2}$        | $226.5 \pm 9.7$       | $223.6 \pm 13.4$                    | $224.3 \pm 7.4$                     |
| $\kappa_3$ , $\text{kpc}$                         | $0.75 \pm 0.12$       | $0.66 \pm 0.25$                     | $0.79 \pm 0.12$                     |

than the current estimate. For example,  $R_0 = 7.0$  kpc in Kuzmin (1956) ( $z_0 = 3.1$  kpc),  $R_0 = 7.2$  kpc in Kuzmin (1953) ( $z_0 = 3.6$  kpc). Additionally, all the mentioned papers considered spherical models, thus decreasing  $z_0$ . The value of  $z_0$  derived by us is close to  $z_0 = 4.8$  kpc, reported by Malasidze (1973).

## 5. DISCUSSION

The options for the procedure of determining model parameters for the potential of the Galaxy from masers considered in this work show that taking into account even a small natural azimuthal velocity dispersion for masers is necessary, given the modern high-accuracy data on these objects. The derived azimuthal dispersion for the joint sample  $\sigma_0 = 6.56 \pm 0.57 \text{ km s}^{-1}$  is intermediary between the radial ( $\sigma_{U,0} = 9.4 \pm 0.9 \text{ km s}^{-1}$ ) and vertical ( $\sigma_{W,0} = 5.9 \pm 0.8 \text{ km s}^{-1}$ ) natural dispersions found by Rastorguev et al. (2017) using almost the same sample, i.e. it agrees with them. However the azimuthal dispersion for the homogeneous HMSFR sample is significantly lower: close values were derived by two methods  $\sigma_{0,1} = 3.9 \pm 0.4$  and  $4.3 \pm 0.4 \text{ km s}^{-1}$  (Table 5). On the other hand, the dispersion for non-HMSFR masers  $\sigma_{0,2} = 15.2 \pm 1.3 \text{ km s}^{-1}$  (even after excluding the anomalous object) is about 3.5–3.9 times higher than for HMSFRs, despite the expected general similarity of these types, which not only confirms the kinematic inhomogeneity of non-HMSFRs compared to HMSFRs, but implies a significant internal inhomogeneity of the non-HMSFR group. The small volume of the non-HMSFR sample ( $N = 32$ ) and the large number of object types there (14 types) do not allow us to determine the dispersion for individual classes.

That said, introducing two natural dispersions for the joint sample lead to a solution without significant shifts of point parameter estimates compared to the results for the

homogeneous HMSFR group, moreover, with smaller statistical parameter errors on the whole. We therefore chose the model with two natural dispersions as the final version for the Stäckel generalization, derived after the exclusion of masers with excessive residuals and the anomalous object (Table 5, approach 2; Fig. 3c).

The derived model rotation curves (Fig. 3) are close to models constructed from masers at  $R > 3\text{--}4$  kpc in Rastorguev et al. (2017); Reid et al. (2019). Our model reconstructs more accurately the decline of the rotation curve in the outer part of the Galaxy than the one in Reid et al. (2019), since the latter a priori used a smoother function form for the model. The model in Rastorguev et al. (2017) reveals more details since they used a polynomial fourth-order model for fitting. A good agreement is achieved in the common  $R$  interval and with the rotation curves based on classical Cepheids in the recent works of Ablimit et al. (2020); Mroz et al. (2019), which also show a slow but steady decreasing velocity trend at,  $R > 6$  kpc. The same is also true for the rotation curve from red giants (Eilers et al., 2019). On the whole, modern rotation curves of the flat subsystems coincide rather well outside of the central region of the Galaxy (see also Bland-Hawthorn and Gerhard (2016)). The halo circular velocity curves derived from Gaia data on RR Lyrae stars (Wegg et al., 2019) are close to our model, especially in the outer part of the galaxy. At  $R < 3$  kpc our model cannot be reliable, if only due to the fact that there it is based on only a few objects, to say nothing of the bar influence (Chemin et al., 2015), but it is still sufficiently close to the rotation curve constructed in the survey by Bland-Hawthorn and Gerhard (2016).

Dynamic modeling in this work was done in the assumption that the average rotation velocity of masers is close to the circular velocity. This assumption agrees with the low azimuthal velocity dispersion which we derived for masers, especially for HMSFRs. Direct estimates of the asymmetric shift for masers are represented by  $\overline{V}_s$  in Reid et al. (2019): they are located in the  $-2 \div -9$  km s<sup>-1</sup> interval for different versions of analysis, but even the most accurate of the estimates,  $\overline{V}_s = -3.1 \pm 2.2$  km s<sup>-1</sup>, does not differ significantly from zero. Similar results were obtained also in Reid et al. (2014). Thus, the asymmetric shift can be neglected for masers, at least with the current level of accuracy.

We used Poisson’s equation to obtain an analytical expression for spatial density for the constructed Stäckel potential [(formulas (5), (10)–(13)] The corresponding equidensities (equal density curves) are presented in Fig. 4 for a density of  $\rho = 0.1 M_\odot \text{pc}^{-3}$ . As is evident from the figure, the halo in the constructed model is non-spherical. The model also does not adequately agree with the modern estimates of the vertical scale of the thin ( $300 \pm 50$  pc) and thick disk ( $900 \pm 180$  pc)(Bland-Hawthorn and Gerhard, 2016).

The derived non-too-realistic equidensities raise the question of the necessity to additionally introduce into the model a vertical distribution of density in one form or another when using Rodionov’s method. I.e., despite the interesting results of Stäckel modeling in a series of theoretical studies (e.g., Kuzmin (1952); Kuzmin and Malasidze (1987); Osipkov (1975)), it turns out that the practical use of such methods in general does not

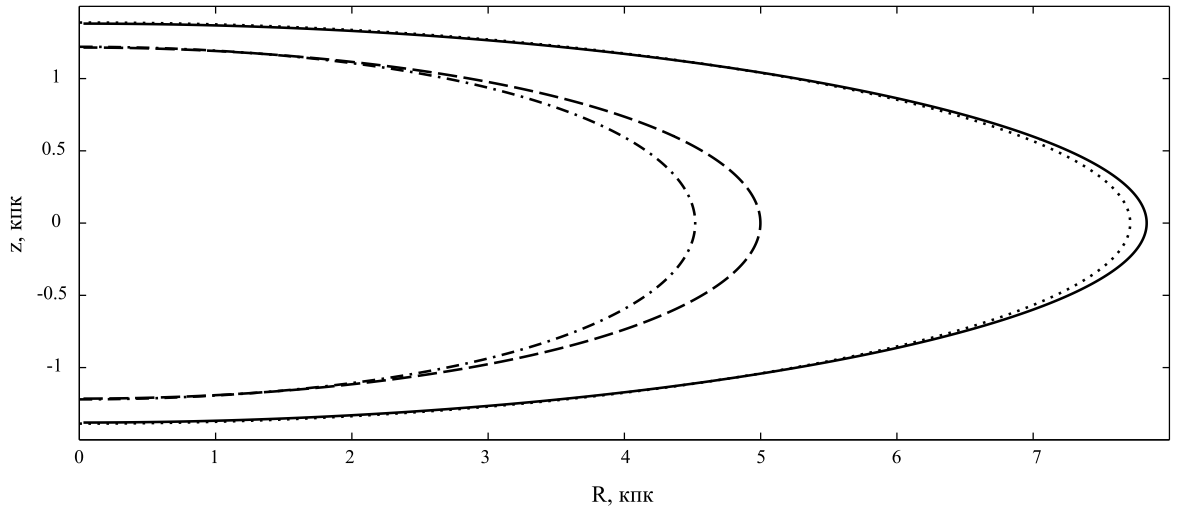


Figure 4: Model equidensites for  $\rho = 0.1 M_{\odot} \text{pc}^{-3}$ . The solid curve is the three-component model; the dashed curve shows the halo; the dotted curve represents the disk, and the dashed-and-dotted curve is the bulge.

lead to a construction of models of acceptable adequacy. We should note that besides some test work carried out by our group (Gromov et al. (2015, 2016)), there were no earlier attempts to use the Stäckel generalization in practice (applicable to real data). Such a result was therefore not obvious. Considering the unrealistic equidensites obtained for disks in Binney and Wong (2017); Famaey and Dejonghe (2003), where other methods of Stäckel modeling were used (including the «Stäckel fudge»), this problem is of a more general nature and not merely a shortcoming of the Stäckel generalization method.

Note that preliminary modeling based on the new catalog of Reid et al. (2019) gives similar results, i.e. the nature of the vertical distribution is data insensitive.

Thus, the vertical structure of the model obtained in this work implies that using a direct Stäckel generalization method is insufficient for constructing realistic Stäckel models. This would require solving the question of accounting for the known properties of the vertical mass distribution in the Galaxy in Stäckel modeling. We considered several approaches and their combinations as possibilities: redefining the function  $\varphi(\xi)$  with account for the vertical distribution; introducing several additional conditions when estimating parameters (for example, we were able to obtain an adequate disk thickness in the assumption of a barometric vertical density distribution in preliminary calculations); varying the parameter  $z_0$  in order to make the shape of the halo more spherical. We propose to study these approaches in our next paper.

For the constructed model the solar neighborhood density ( $R_0 = 8.34 \text{ kpc}$  [32])  $\rho_{\odot} = 0.082 M_{\odot} \text{pc}^{-3}$  is in good agreement with the current estimates:  $\rho_{\odot} = 0.08\text{--}0.11 M_{\odot} \text{pc}^{-3}$  (Loktin and Marsakov, 2009),  $\rho_{\odot} = 0.097 \pm 0.013 M_{\odot} \text{pc}^{-3}$  (Bland-Hawthorn and Gerhard, 2016).

The model mass in a sphere of 50 kpc radius is  $M_{50} = 0.82 \times 10^{12} M_{\odot}$ , which is somewhat higher than in the other studies. For example, Deason et al. (2012) found

$M_{50} = (0.42 \pm 0.04) \times 10^{12} M_{\odot}$ , and Williams and Evans (2015) —  $M_{50} = (0.45 \pm 0.15) \times 10^{12} M_{\odot}$ . The model mass in a 20 kpc sphere turned out equal to  $0.35 \times 10^{12} M_{\odot}$ . The overestimated masses are probably also linked to omitting the data on the vertical density distribution.

## 6. CONCLUSIONS

We constructed an analytical three component Stäckel model of the Galaxy using the data on masers with trigonometric parallaxes, proper motions, and radial velocities.

The maser data were used to estimate the parameters of the components — halo, disk, and bulge — for a model representing the potential in the Galactic plane. We show that non-HMSFR masers, i.e., masers not related to high-mass star forming regions (HMSFRs), are kinematically inhomogeneous with respect to HMSFR masers: the natural (non-instrumental) dispersion of their azimuthal velocity components,  $\sigma_{0,2} = 15.2 \pm 1.3 \text{ km s}^{-1}$  in 3.5–3.9 times higher than the similar dispersion  $\sigma_{0,1} = (3.9 \div 4.3) \pm 0.4 \text{ km s}^{-1}$  for HMSFRs. This fact should be taken into account when using data on the kinematics of inhomogeneous maser types. The final model was obtained with account for the difference in natural dispersions for these two groups — HMSFRs and non-HMSFRs. The model circular velocity curve is in good agreement with the observed data.

The derived model of the Galactic plane potential served as a basis for constructing a Stäckel model of the Galaxy using Rodionov’s method (Rodionov, 1974), which allows us to determine the values of the potential in the entire space. The model gives close to real values of the density in the solar neighborhood of  $\rho_{\odot} = 0.082 M_{\odot} \text{ pc}^{-3}$  and the total mass of  $M_{50} = 0.82 \times 10^{12} M_{\odot}$  (accurate to an order of magnitude). However, the nature of equidensities in the meridian plane of the model shows that direct use of the Stäckel generalization method alone is not enough to construct realistic Stäckel models. To that end, one needs to develop methods of directly accounting for data on the vertical density distribution in the Galaxy when using Rodionov’s method.

Despite the uncovered but solvable complication, the approach on the whole has significant potential: the proposed simple and, especially, analytical method of computing function  $\varphi(\xi)$  of the Stäckel potential can be used when finding actions and may significantly simplify the corresponding algorithms of constructing the phase model of the Galaxy.

The authors are grateful to V.V. Bobylev for providing the information on three masers with full data and A.V. Veselova for the help with data reduction, and especially for the complex task of identifying object types. The authors are grateful to the anonymous referee for useful comments.

## 7. FUNDING

The reported study was funded by RFBR, project number 19-32-90144.

## 8. CONFLICT OF INTEREST

The authors declare no conflict of interest.

## References

1. I. Ablimit, G. Zhao, C. Flynn, and S. A. Bird, *Astrophys. J.* **895** (1), L12 (2020).
2. J. Binney, *Monthly Notices Royal Astron. Soc.* **401** (4), 2318 (2010).
3. J. Binney, *Monthly Notices Royal Astron. Soc.* **426** (2), 1324 (2012).
4. J. Binney and M. Merrifield, *Galactic Astronomy* (Princeton University Press, Princeton, NJ, 1998).
5. J. Binney and L. K. Wong, *Monthly Notices Royal Astron. Soc.* **467** (2), 2446 (2017).
6. J. Binney, R. L. Davies, and G. D. Illingworth, *Astrophys. J.* **361**, 78 (1990).
7. J. Bland-Hawthorn and O. Gerhard, *Annual Rev. Astron. Astrophys.* **54**, 529 (2016).
8. N. A. Bond, Z. Ivezić, B. Sesar, et al., *Astrophys. J.* **716** (1), 1 (2010).
9. R. A. Burns, T. Handa, H. Imai, et al., *Monthly Notices Royal Astron. Soc.* **467** (2), 2367 (2017).
10. L. Chemin, F. Renaud, and C. Soubiran, *Astron. and Astrophys.* **578**, A14 (2015).
11. J. O. Chibueze, H. Hamabata, T. Nagayama, et al., *Monthly Notices Royal Astron. Soc.* **466** (4), 4530 (2017).
12. J. O. Chibueze, H. Sakanoue, T. Nagayama, et al., *Publ. Astron. Soc. Japan* **66** (6), 104 (2014).
13. A. J. Deason, V. Belokurov, N. W. Evans, and J. An, *Monthly Notices Royal Astron. Soc.* **424** (1), L44 (2012).
14. W. Dehnen, *Astron. J.* **118** (3), 1201 (1999).
15. A. S. Eddington, *Monthly Notices Royal Astron. Soc.* **76**, 37 (1915).
16. A.-C. Eilers, D. W. Hogg, H.-W. Rix, and M. K. Ness, *Astrophys. J.* **871** (1), 120 (2019).
17. J. Einasto and U. Rummel, *Astrophysics* **6** (2), 120 (1970).
18. B. Famaey and H. Dejonghe, *Monthly Notices Royal Astron. Soc.* **340** (3), 752 (2003).

19. E. Gardner, P. Nurmi, C. Flynn, and S. Mikkola, *Monthly Notices Royal Astron. Soc.* **411** (2), 947 (2011).
20. A. O. Gromov, I. I. Nikiforov, and L. P. Ossipkov, *Baltic Astronomy* **24**, 150 (2015).
21. A. O. Gromov, I. I. Nikiforov, and L. P. Ossipkov, *Baltic Astronomy* **25**, 53 (2016).
22. M. Henon and C. Heiles, *Astron. J.* **69**, 73 (1964).
23. L. Hernquist, *Astrophys. J.* **356**, 359 (1990).
24. G. Hori, *Publ. Astron. Soc. Japan* **14**, 353 (1962).
25. M. Kaasalainen and J. Binney, *Monthly Notices Royal Astron. Soc.* **268**, 1033 (1994).
26. G. G. Kuzmin, *Publ. Tartu Astrofiz. Obs.* **32**, 332 (1952).
27. G. G. Kuzmin, *Izvestiya Akad. Nauk ESSR* **2**, 3 (1953).
28. G. G. Kuzmin, *Astron. Zh.* **33**, 27 (1956).
29. G. G. Kuzmin and G. A. Malasidze, *Akademiia Nauk Gruzinskoj SSR* **54**, 565 (1969).
30. G. G. Kuzmin and G. A. Malasidze, *Publ. Tartu Astrofiz. Obs.* **52**, 48 (1987).
31. G. G. Kuzmin, U. I. K. Veltmann, and P. L. Tenjes, *Publ. Tartu Astrofiz. Obs.* **51**, 232 (1986).
32. A. V. Loktin and Marsakov V. A., *Lecscii po zvezdnoi astronomii* (SFedU, Rostov-na-Dony, 2009).
33. G. A. Malasidze, *Proc. conf. on Dynamics of Galaxies and Star Clusters*, pp. 93–98 (1973).
34. M. R. Merrifield, *Astron. J.* **102**, 1335 (1991).
35. P. Mroz, A. Udalski, D. M. Skowron, et al., *Astrophys. J.* **870** (1), L10 (2019).
36. I. I. Nikiforov, *Astron. and Astrophys. Transact.* **27** (3), 537 (2012).
37. I. I. Nikiforov and A. V. Veselova, *Astr. Lett.* **44** (11), 699 (2018).
38. K. F. Ogorodnikov, *Dinamika zvezdnykh sistem* (Gosydarstvennoe izdatel'stvo fiziko-matematichskoi literatury, Moskva, 1958) [in Russian].
39. L. P. Osipkov, in *Vestnik Leningradskogo Universiteta. Seriya 1. Matematika. Mekhanika. Astronomiia*, pp. 151–158 (1975) [in Russian].
40. L. Posti, J. Binney, C. Nipoti, and L. Ciotti, *Monthly Notices Royal Astron. Soc.* **447** (4), 3060 (2015).

41. A. S. Rastorguev, N. D. Utkin, M. V. Zabolotskikh, et al., *Astrophysical Bulletin* **72** (2), 122 (2017).
42. M. J. Reid, K. M. Menten, A. Brunthaler, et al., *Astrophys. J.* **885** (2), 131 (2019).
43. V. I. Rodionov, in *Vestnik Leningradskogo Universiteta. Seriya 1. Matematika. Mekhanika. Astronomiia*, pp. 142–148 (1974) [in Russian].
44. J. Sanders, *Monthly Notices Royal Astron. Soc.* **426** (1), 128 (2012).
45. J. Sanders and J. Binney, *Monthly Notices Royal Astron. Soc.* **457** (2), 2107 (2016).
46. M. J. Reid, K. M. Menten, A. Brunthaler, et al., *Astrophys. J.* **793** (2), 72 (2014).
47. C. Satoh and M. Miyamoto, *Publ. Astron. Soc. Japan* **28** (4), 599 (1976).
48. P. Stäckel, *Math. Annal.* **35**, 91 (1890).
49. C. Wegg, O. Gerhard, and M. Bieth, *Monthly Notices Royal Astron. Soc.* **485** (3), 3296 (2019).
50. A. A. Williams and N. W. Evans, *Monthly Notices Royal Astron. Soc.* **454** (1), 698 (2015).